The accommodation of the south flank's motion by the Koa'e fault system, Kīlauea, Hawai'i: insights from the June 2012 earthquake sequence

Shuangyu Ge[1], Guoqing Lin[1*], Falk Amelung[1], Paul G. Okubo[2], Donald A. Swanson[2], and Zhang Yunjun[1]

[1]Department of Marine Geosciences, Rosenstiel School of Marine and Atmospheric Science, University of Miami, Miami, Florida, USA.

[2]Hawaiian Volcano Observatory, U.S. Geological Survey, Hawai'i, USA.

Corresponding author: Guoqing Lin, glin@rsmas.miami.edu

[*]4600 Rickenbacker Causeway, Miami, FL, 33149

Key Points:

- This paper presents an explicit model of two faults in the central part of the Koa'e fault system based on the geophysical and geological analyses and modeling.
- This paper provides a new perspective of the normal-fault-evolution in the Koa'e fault system associated with slow slip events and the accommodation of the south flank's motion, Kīlauea.

Abstract

The Koa‘e fault system is a prominent and complex structural element of Kīlauea volcano, Hawai‘i. On June 5, 2012, a sequence of shallow earthquakes occurred in the central part of the Koa‘e fault system. The InSAR data from multiple satellites spanning the time of the earthquake occurrence indicate a maximum of ~10 cm surface displacement above the seismic events in the Koa‘e. The GPS data from multiple stations show that there was a slow slip event in the south flank in late May 2012. Field visits to the fault after the earthquakes revealed ground cracks. In this study, we combine the seismic, InSAR, GPS data, and field observations to investigate the characteristics of the Koa‘e fault system. We relocate the seismic events in the central part of the Koa‘e fault system, compute the focal mechanisms for the events in the June 2012 earthquake sequence, invert for a two-fault model based on the surface deformation, and discuss their relationships with the 2012 slow slip event. Based on our Coulomb stress change calculation, we infer that the 2012 slow slip event may have triggered both the seismic events and the surface deformation and played a major role in the evolution of the Koa‘e fault system and the accommodation of the south flank’s motion. Our integrated analyses are helpful to constrain the fault geometry in the Koa‘e system and to shed light on the role of Koa‘e in the structural evolution of Kīlauea.

1 Introduction

Kīlauea volcano (Figure 1) on the southeastern part of the island of Hawai‘i is noted for its volcanic activity, ongoing structural evolution, and related seismicity. High-precision earthquake locations help define the internal structures of the volcano (e.g., Klein et al., 1987; Got et al., 1994; Denlinger and Okubo, 1995; Gillard et al., 1996; Rubin et al., 1998; Battaglia et al., 2003; Got and Okubo, 2003; Wolfe et al., 2003, 2004, 2007; Park et al., 2009; Syracuse et al., 2010; Matoza et al., 2013; Lin et al., 2014). Shallow seismic events (3-5 km below the ground surface) indicate magma activity within the summit and rift zones (Wright and Klein, 2006), and deep earthquakes (8-12 km) denote the seaward motion along the décollement fault (e.g., Tilling and Dvorak, 1993; Denlinger and Okubo, 1995; Park et al., 2009; Syracuse et al., 2010; Lin et al., 2014). Within the intrusive growth of Kīlauea, the seaward motion of its south flank (up to ~8 cm/yr, Owen et al., 2000; Miklius et al., 2005) plays a key role in its evolution. This seaward motion can be accommodated via three primary methods: magmatic intrusions, earthquakes, and aseismic slip events (Miklius et al., 2005). In 1975, the largest measured seaward displacement of the south flank reached about 8 m horizontally generated by the Mw7.4 Kalapana earthquake (Lipman et al., 1985; Cannon et al., 2001). More recently, an M6.1 earthquake in 1989 (Árnadóttir et al., 1991) and another M6.9 earthquake in 2018 struck the south flank. Since the installation of the continuous GPS network on the island of Hawai‘i in 1996, more than ten slow slip events, a major form of seaward motion, have been detected under the south flank (Montgomery-Brown et al., 2013). These slow slip events occurred along the décollement fault, which is about 8 km deep beneath the south flank and often considered as the base of the volcanic edifice (Montgomery-Brown et al., 2015). Note that the ground surface in our study area is about 1 km above sea level (Figure 2a). All the depths throughout this paper are relative

62 to the ground surface.

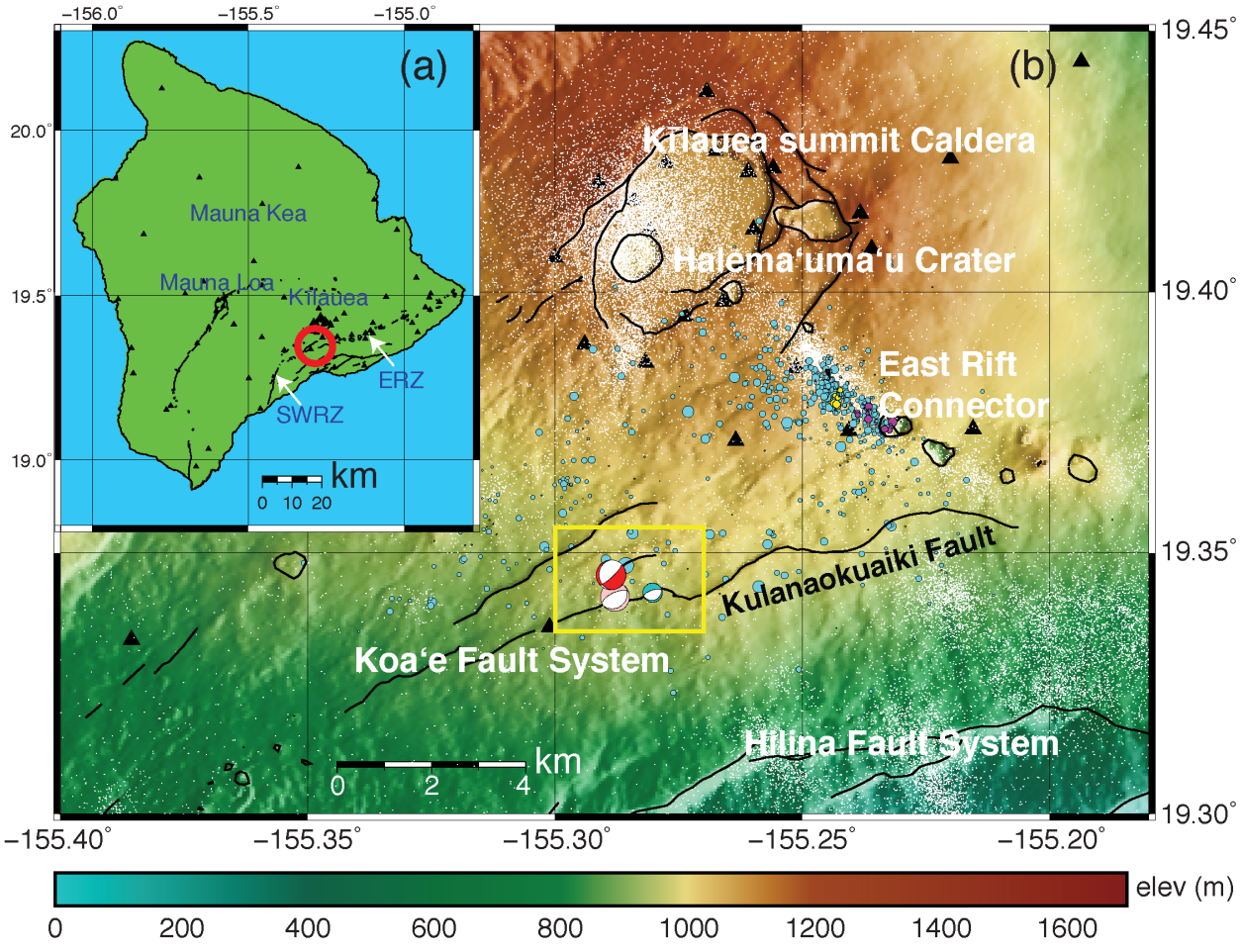

63

64 **Figure 1**. (a) The island of Hawai'i with our study area, the Koa'e fault system, enclosed by the
65 red circle. Abbreviations are ERZ, East Rift Zone; and SWRZ, Southwest Rift Zone. (b) Precise
66 earthquake locations in our study area recorded by the HVO seismic stations. Black triangles are
67 the HVO stations. White dots are the background seismicity from 1992 to 2009 (Lin et al., 2014).
68 Cyan circles represent the 3-D relocated earthquakes between 2009 and 2014. Purple and yellow
69 circles in the East Rift Connector are the two earthquake clusters identified by waveform cross-
70 correlation. The size of each circle is proportional to the event magnitude. The yellow box
71 encloses the area with the detected surface deformation shown in Figure 2. Three beach balls are
72 the preferred focal solutions of the seismic events on June 5, 2012 with the red one for the M3.6
73 event and pink and blue ones for the first two events. The Kulanaokuaiki Fault is the longest
74 fault and the southern boundary of the Koa'e fault system. The background topography is
75 downloaded from the Hawaiian multibeam bathymetry synthesis
76 (http://www.soest.hawaii.edu/hmrg/multibeam).
77

The "driving force" of the seaward motion could be explained by dike intrusions at 4-10 km deep below the ground surface into both the East Rift Zone and the Southwest Rift Zone in the upper part of the edifice (Cayol et al., 2000) and/or gravitational spreading of a magma mush (Denlinger and Okubo, 1995; Borgia et al., 2000; Plattner et al., 2013). However, it is not fully understood how the deformation is accommodated in the shallow zone near the surface. A suitable site to investigate this is the primary surface boundary between Kīlauea's summit caldera and its south flank. This boundary consists of the Koa'e fault system, the East Rift Zone, and the southwest rift zone (Figure 1). As one part of the boundary, the Koa'e fault system may play a key role in accommodating the flank motion. It also serves as a natural lab to study the geometry and formation of normal faults in tensile environments (Peacock and Parfitt, 2002; Martel and Langley, 2006; Podolsky and Roberts, 2008; Bubeck et al., 2014). Duffield (1975) presented a detailed structural map for part of the Koa'e fault system and suggested an origin from the forceful injection of dikes in the rift zones. Peacock and Parfitt (2002) observed active relay ramps and hypothesized the evolutionary stages of the Koa'e fault system. Martel and Langley (2006) combined the field observations and mechanical analyses to infer the propagation of normal faults to the surface. Holland et al. (2006) also applied the scaled model experiments to simulate the fault structures in the Koa'e fault system. However, no quantitative models have been provided for any specific fault in the Koa'e fault system due to the lack of appropriate seismic and InSAR data.

On June 5, 2012, a sequence of three earthquakes occurred in the shallow (1.8-2.1 km below the ground surface) central part of the Koa'e fault system. InSAR data revealed surface deformation in the same area (Swanson et al., 2018) between June 2 and June 8, given by the acquisition times of the SAR images. The earthquake sequence and the detected surface

101 deformation provide an excellent opportunity to explore the detailed geometry and evolution of
102 the Koa‘e fault system. In this study, we used precise earthquake relocations, focal mechanisms,
103 geodetic modeling, and field observations to examine the characteristics of the Koa‘e fault
104 system and its role in the accommodation of the south flank’s motion in Kīlauea.

105 **2 Geologic Setting**

106 Kīlauea’s main structural features consist of the summit caldera, the East Rift Connector
107 (Swanson et al., 2018), the East Rift Zone (ERZ), and the Southwest Rift Zone (SWRZ) (Figure
108 1). The East Rift Connector extends from the summit caldera towards southeast, and the East
109 Rift Zone extends east-northeast from the point where the connector meets the Koa‘e fault
110 system. The Southwest Rift Zone extends southwestward from the summit caldera. The 20 km-
111 long and 2.5 km-wide Koa‘e fault system is located about 5 km south of the summit caldera
112 (Duffield, 1975) with an average elevation of 1 km above sea level. The Koa‘e fault system
113 connects the middle SWRZ with the ERZ and structurally separates the summit area from the
114 south flank. It contains many cracks, normal fault segments and mostly north-facing scarps
115 (Duffield, 1975; Wolfe and Morris, 1996; Martel and Langley, 2006).

116 The southernmost fault of the Koa‘e fault system is the 15 km long, east-northeast
117 striking Kulanaokuaiki Fault with a scarp facing north-northwest (Figures 1 and 2) (Martel and
118 Langley, 2006). The Kulanaokuaiki Fault is named after the official geographic term
119 “Kulanaokuaiki Pali” (pali means cliff in the Hawaiian language) in the Koa‘e fault system.
120 About 0.75 km north of the Kulanaokuaiki is the east-northeast striking Ohale Fault area (Martel
121 and Langley, 2006). This area contains numerous cracks and south-facing low scarps (Martel and
122 Langley, 2006), in contrast to the majority of the north-northwest facing high scarps in the

broader Koa'e area. We here refer to "low" and "high" scarps with heights of less or more than 5 m, respectively. The major (or largest) scarp in the Ohale Fault area also dips south-southeast. An unnamed, several kilometers long fault (the Ohale pali in Avery et al., 2002) is located about 0.3 km north of the Ohale Fault (the upper left corner in Figure 2a), which also strikes east-northeast and has a north-facing scarp.

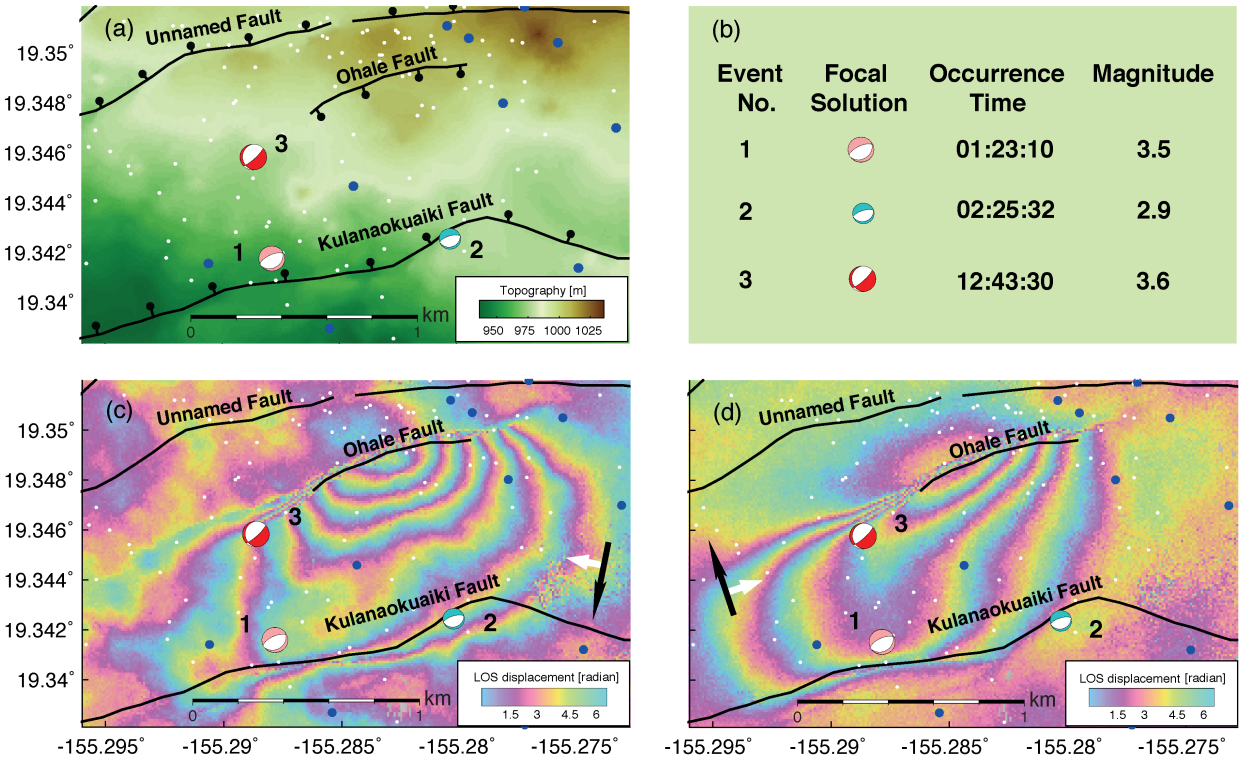

Figure 2. (a) The preferred focal solutions of the three earthquakes on June 5, 2012 in the area of the Ohale Fault and the Kulanaokuaiki Fault (pink, blue and red beach balls for the M3.5, M2.9 and M3.6 events). Black lines show three active faults with ball-and-bar symbols on the hanging walls. The background is the topographic mapping. (b) Information of the three seismic events: preferred focal solution, occurrence time, and magnitude. (c, d) Line-of-Sight (LOS) displacement (between June 2 and June 8, 2012) from descending (c) and (d) ascending satellite tracks. Fault lines are the three major surface fault traces digitized from the Geological Map of the Island of Hawai'i (Wolfe and Morris, 1996). White dots are the background seismicity from 1992 to 2009 (Lin et al., 2014). Blue circles are the 3-D relocated events whose depths are less than 9 km beneath the ground surface from March 2009 to June 2014. The size of each circle is proportional to the event magnitude. The black arrows show the satellite flight direction and the white arrows perpendicular to them are the satellite look direction.

3 Data and Processing

3.1 Seismic Analyses

We acquired the seismic data from April 2009 to June 2014 near the Koa‘e fault system from the U.S. Geological Survey (USGS) Hawaiian Volcano Observatory (HVO). A total of 746 earthquakes were processed using the three-dimensional (3-D) ray tracing through the seismic velocity model by Lin et al. (2014) to obtain better-constrained absolute locations. We resampled the waveform data of the 3-D relocated events at 100 Hz sample rate and band-pass filtered them from 1 to 10 Hz (Lin et al., 2007). We then applied the Delaunay tessellation to seismic event pairs within 5 km for natural neighboring event detection (Richards-Dinger and Shearer, 2000). Correlation coefficients for neighboring events were calculated to select qualified event pairs to conduct the relative relocation. We used time windows of 1.5 s for P wave and 2.5 s for S wave if the network arrivals are available. If not, we used 2 s for P wave and 3 s for S wave instead (Lin et al., 2007). We only chose event pairs with an average correlation coefficient over 0.55 from all available differential times and 0.6 from at least eight differential times. Using these qualified event pairs and the corresponding cross-correlation results, we grouped earthquakes into different clusters by applying similar-event cluster analysis (Shearer et al., 2005). Within each cluster, differential times calculated from cross-correlation were used to relocate each event to obtain more precise relative location based on a one-dimensional velocity model (Lin et al., 2014). This differential time relocation method is described in detail by Lin et al. (2007) and Lin (2018). Based on the earthquake relocations, we computed focal mechanisms from *P*-wave first

motion polarity observations by applying the HASH program (Hardebeck and Shearer, 2002), similar to Lin and Okubo (2016).

3.2 Deformation Data

We used synthetic aperture radar (SAR) data from both descending track 165 and ascending track 10 of the COSMO-SkyMed satellites from May 1 to June 30, 2012 from the Hawaiian Volcano Supersite and processed them using the JPL/Caltech's ISCE software (Rosen et al., 2012). We used the 1/3 arc-second digital elevation model data (DEM with 10 m precision) from the National Map Viewer at the U.S. Geological Survey (https://viewer.nationalmap.gov/viewer/) to remove topographic phase contributions and generated all possible interferograms. With the assistance of additional Radarsat-2 satellite data, the data-pairs show that the deformation happened between June 2 and June 8 in 2012. Figure 2 shows the surface deformation during this time period in the central part of the Koa'e fault system.

To specify the exact deformation time, we acquired the GPS data in the study area from the Nevada Geodetic Laboratory GPS Networks. Unfortunately, the nearest GPS stations did not show any coseismic signal. Thus, we selected the May 29 to June 17 interferogram from the ascending track and the May 7 to June 24 interferogram from the descending track for detailed analyses. However, the GPS data revealed the occurrence of a large-scale slow slip event in late May 2012. This event occurred along the décollement under the south flank on May 28, 2012 and lasted for about two days, accompanied by a ~2.5 cm opening in the East Rift Zone (Montgomery-Brown et al., 2015).

4 Results

4.1 Seismic Relocation and Focal Mechanisms

The June 5, 2012 seismic sequence consisted of three earthquakes in the area near the Ohale and the Kulanaokuaiki Faults (beach balls in Figure 1). The first event with a local magnitude of 3.5 occurred at 1:23 am Coordinated Universal Time (UTC) and is located about 150 m north of the surface trace of the Kulanaokuaiki Fault. The second event with a magnitude of 2.9 occurred one hour later and is positioned ~1 km to the east. Another 10 hours later, the third event of magnitude 3.6 took place ~500 m north of the first two events, southwest of the surface trace of the Ohale Fault. The relocated depths of the three events were about 2 km below the ground surface (1.8 km, 1.93 km, and 2.08 km, respectively). The horizontal and vertical uncertainties of absolute locations for the three earthquakes are (26 m, 24 m, 24 m) in the east-west direction, (34 m, 19 m, 33 m) in the north-south direction, and (54 m, 34 m, 67 m) in the vertical direction, respectively.

Because of the non-uniqueness in focal mechanism inversion, we obtained nine possible focal solutions for the three earthquakes (five for the first one, two for the second, and two for the third). As each beach ball contains two fault planes, we thus considered 18 possible fault solutions. Based on the qualities of these solutions (defined by the HASH program) and the local geological setting, we selected the preferred solution for each event (details available in the supplemental text S1-S2). For the first two events, the inferred fault planes from the preferred focal solutions are consistent with each other. Both are normal-fault planes facing north-northwest and have similar angles of dip (65° and 67°) and strike (246° and 252°, east-

205 northeast). For the third event, the selected fault plane is also a normal type striking northeast but
206 facing southeast. The three chosen focal solutions are shown in Figure 2 and Table 1.

207 **Table 1.** Parameters of the seismic sequence on June 5, 2012 with their preferred focal solutions.
208

Event No.	Time (UTC)	Strike (°)	Dip (°)	Rake (°)	Longitude (°)	Latitude (°)	Depth[1] (km)	Local Magnitude
1	1:23	246	65	-83	-155.2878	19.3417	1.80	3.5
2	2:25	252	67	-89	-155.2803	19.3423	1.93	2.9
3	12:43	47	78	-74	-155.2887	19.3458	2.08	3.6

209 [1]Depth is relative to the ground surface.
210

211 **4.2 Surface Deformation**

212 The surface deformation was detected over a zone approximately 2 km long and 0.8 km
213 wide near the Ohale and the Kulanaokuaiki Faults. The maximum displacement of 10 cm in
214 Line-of-Sight (LOS) direction occurred in both ascending and descending data at the Ohale Fault
215 (Figure 2c and d). In the Ohale Fault area, the phase discontinuity over a length of 1 km indicates
216 a surface rupture. A small phase discontinuity (about one deformation pattern or color cycle
217 disappearance) indicates another surface fracturing of several centimeters near the Kulanaokuaiki
218 Fault (Figure 2c and d).
219

220 **4.3 Geodetic Modeling**

221 We next applied geodetic inverse modeling to find the best-fitting homogeneous elastic
222 dislocation models (Okada, 1992) that are consistent with our observations (Figure 3a and b). We
223 used the University of Miami's Matlab-based Geodetic Modeling Software (Geodmod). We
224 sampled the two interferograms in the target area into uniform 50×50 grids (Figure S1 in the
225 supplementary material) and weighted the InSAR data within each grid equally. We then
226 calculated the root mean square (RMS) of the misfit ($\sqrt{\sum_{i=1}^{N}(\boldsymbol{d_i} - \boldsymbol{m_i})^2 / \boldsymbol{N}}$), where $\boldsymbol{N}$ is the total
227 number of data points, $\boldsymbol{d_i}$ is the observed displacement, and $\boldsymbol{m_i}$ is the predicted displacement
228 calculated by the dislocation model in an elastic half-space. We used the Monte Carlo-based
229 Gibbs sampling algorithm (Brooks and Neil Frazer, 2005; Baker and Amelung, 2012) to obtain
230 the optimal model by searching for the minimum RMS.

231 We first considered a one-fault model (Fault A) and inverted for ten parameters of the
232 fault (length, width, depth, dip, strike, longitude, latitude, strike-slip, dip-slip, opening). The
233 length refers to the length measurement of the top edge in the fault model. The width measures
234 down-dip extent of the fault plane. The depth is measured at the top edge of the fault plane and
235 was fixed at 0 km (i.e., the ground surface) in this study. The opening component of the fault was
236 fixed as zero based on the preliminary results suggesting minimal opening. The best-fitting fault
237 (Fault A) strikes WSW-ENE and dips 62° towards the south-southeast with a normal dip-slip of
238 11 cm and a right-lateral strike-slip of 2 cm (Figure 3c and d). In order to fit the second phase
239 discontinuity near the Kulanaokuaiki Fault observed in the InSAR data (Figure 2c and d), we
240 then examined a two-fault model. While fixing the parameters of the first fault (Fault A), we
241 searched for the ten parameters for a second fault (Fault B) within 0.5 km of the phase

discontinuity at the Kulanaokuaiki Fault. The depth and the opening component were also fixed at the same values as those for Fault A. The strike-slip component was also set as zero based on the preliminary results suggesting minimal strike-slip. The best-fitting geometry coincides with the surface trace of the Kulanaokuaiki Fault (Figure 3e and f). In this two-fault model, Fault B strikes ENE-WSW direction and has an NNW dip angle of 77° and a normal dip-slip of 3 cm. Compared with the one-fault model, the two-fault model fits the data better (RMS of 7.6 mm compared with 8.6 mm, Table 2) and has a narrower displacement residual distribution (Figure S2 in the supplementary material). We also performed the F-test (Boxenbaum et al., 1974; Menke, 1989; Ludden et al., 1994) to confirm that the two-fault model fits the data better than the one-fault model at a 95% confidence level when the number of model parameters is taken into consideration (supplementary text S1).

In the modeling of Fault B, we have no robust constraints on neither dip angle nor width. In order to obtain the optimal two-fault model, we constrained the inversion ranges of the dip angle and the width in the Geodmod. We have three requirements for the selection of the best model: (1) an RMS at the minimum level of 7.6 mm; (2) no physically implausible intersecting structure; and (3) a similar structure as in the scaled model experiments (Holland et al., 2006). In our final model, Fault A and Fault B contact slightly and form the borders of a graben structure (Figure 4). This model is supported by the general interpretation that the Koa‘e is a system of grabens (Duffield, 1975). The width of Fault B is at least 1.0 km and could extend deeper.

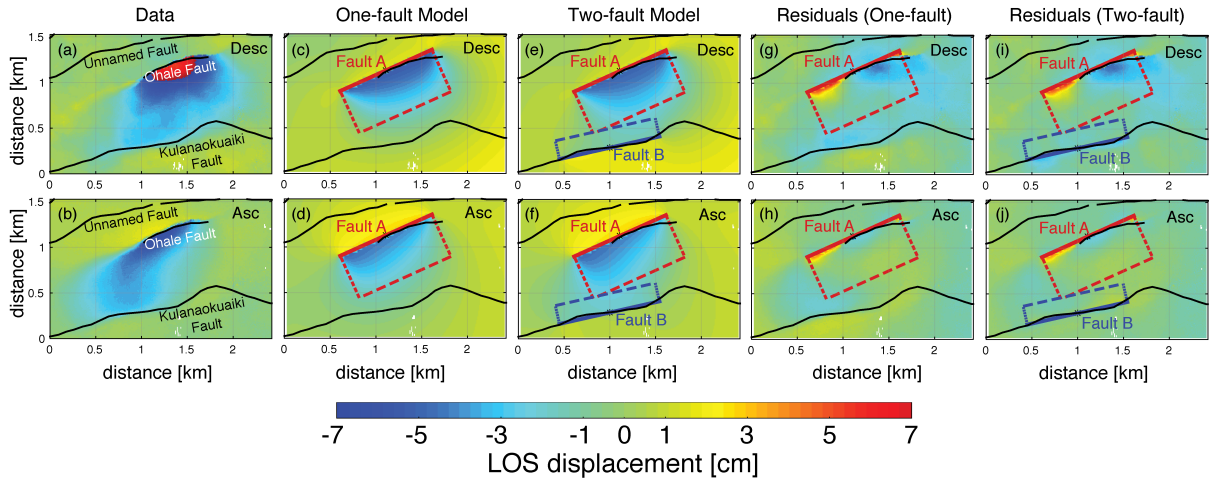

Figure 3. (a, b) Observed LOS displacement on the surface from the descending and ascending tracks, respectively. (c, d) Displacements of the one-fault model. (e, f) Displacements of the two-fault model. (g, h) Displacement residuals of the one-fault model. (i, j) Displacement residuals of the two-fault model. Solid lines in (c-j) are the surface traces of the two modeled faults, whereas dashed ones are the other boundaries of the faults projected on the surface. Red lines show the first fault (Fault A) facing southeast, and blue lines show the second fault (Fault B) facing northwest.

271 **Table 2.** Parameters and their corresponding uncertainties in the geodetic fault modeling.

272

Fault No.	Length (km)	Width (km)	Depth[1] (km) fixed	Dip (°)	Rake (°)	Strike (°)	Longitude (°)	Latitude (°)	Dip-slip (cm)	Strike-slip[2] (cm)	RMS (mm)
One-fault model											
A[3]	1.1 ±0.1	1.1 ±0.1	0	62 ±2	-100 ±1	66 ±1	-155.2853 ±0.0001	19.3483 ±0.0001	11.0 ±0.1	-2.0 ±0.1	
											8.6
Two-fault model											
A[4]	1.1	1.1	0	62	-100	66	-155.2853	19.3483	11	-2	
B	1.1 ±0.2	1.0 ±0.1	0	77 ±2	-90	257 ±3	-155.2865 ±0.0001	19.3406 ±0.0001	3.0 ±0.1	0	
											7.6

273 [1]Depth refers to the depth of the top edge of each fault plane; zero indicates the ground surface.

274 [2]The negative value indicates the right-lateral strike-slip.

275 [3]Each parameter consists of the best fitting value and the corresponding uncertainties (2σ). The
276 standard deviation (σ) is calculated from the Gaussian probability density distribution based on
277 the Gibbs sampling for the parameters of Fault A.

278 [4]The parameters of Fault A are fixed at the best fitting values from one-fault model.

279

280 The best-fitting two-fault geodetic model can be visualized in Figure 4. The red south-
281 southeast facing rectangle represents the major plane Fault A in the Ohale Fault area, and the
282 blue north-northwest facing rectangle represents Fault B coinciding with the Kulanaokuaiki

Fault. We have no sufficient geodetic data or solid geological evidence to constrain the width of Fault B, which is discussed in a later section.

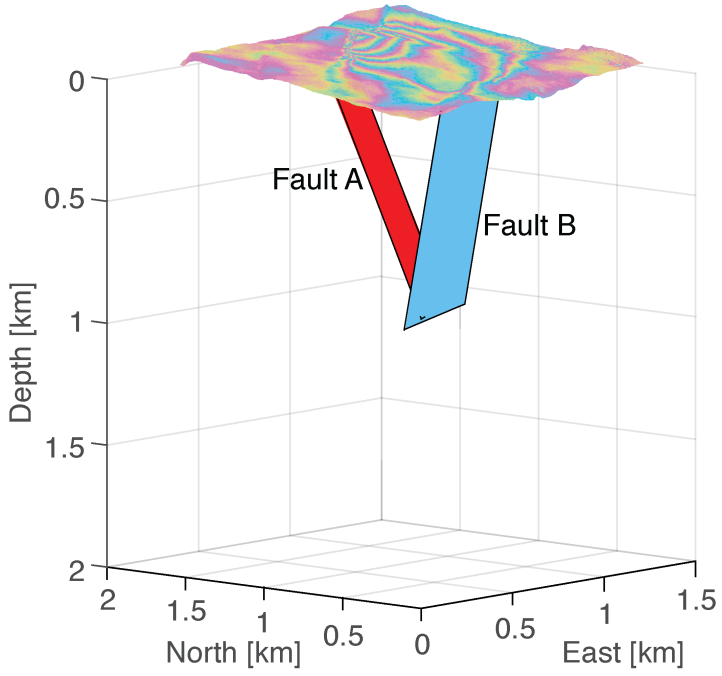

Figure 4. The two-fault model with the InSAR image above. Red fault (Fault A) shows the major fault facing southeast in the Ohale Fault area. Blue fault (Fault B) shows the second fault facing northwest in the Kulanaokuaiki Fault. Zero km indicates the ground surface. The upper edges of the two fault planes are at 1 km above mean sea level.

4.4 Field Observations

In order to confirm the location and geometry of the modeled faults, we visited the area of the 2012 sequence in July 2017, with the focus on the area close to the maximum surface displacement shown in Figure 2. We mapped this area using a GARMIN navigator with an accuracy of about 6 m and found that it was not characterized by a single fault, but an elongated, narrow (~50 m wide) fault area with low scarps and ground cracks. These cracks were formed before the deformation in our study and vary from several centimeters to over a meter in their

298 widths. A field investigation conducted on June 22, 2012 found no new cracking of basalt flows,
299 but only a few cracks several millimeters wide in alluvium and old volcanic ash deposits
300 (Swanson et al., 2018). However, it is possible that some cracks eroded after the surface
301 deformation and before June 22, 2012. We began our measurements for the boundary of the
302 Ohale Fault area in its easternmost part by following one major ground fracture. The starting
303 point is about 200 m southwest of the Ohale benchmark, which is the geographic reference point
304 in the area. The beginning part of the major fracture is a south-facing scarp 1-2 m high with a
305 length of over 10 m (Figure 5b). The fractures split and merge repeatedly on the footwall side of
306 the Ohale Fault area. Where one fracture ends, the largest neighboring fissure was followed and
307 marked (Figure 5c). Our field results show that the Ohale Fault area is one of the relatively few
308 areas in the Koa‘e fault system that have low palis with south-facing scarps, consistent with the
309 inferred southward dip of Fault A in the geodetic two-fault model. In general, the field
310 observations of the Ohale and Kulanaokuaiki Faults are in high accordance with our geodetic
311 model of the two opposite faults inverted from the InSAR data without any a priori reference of
312 geological setting.

313

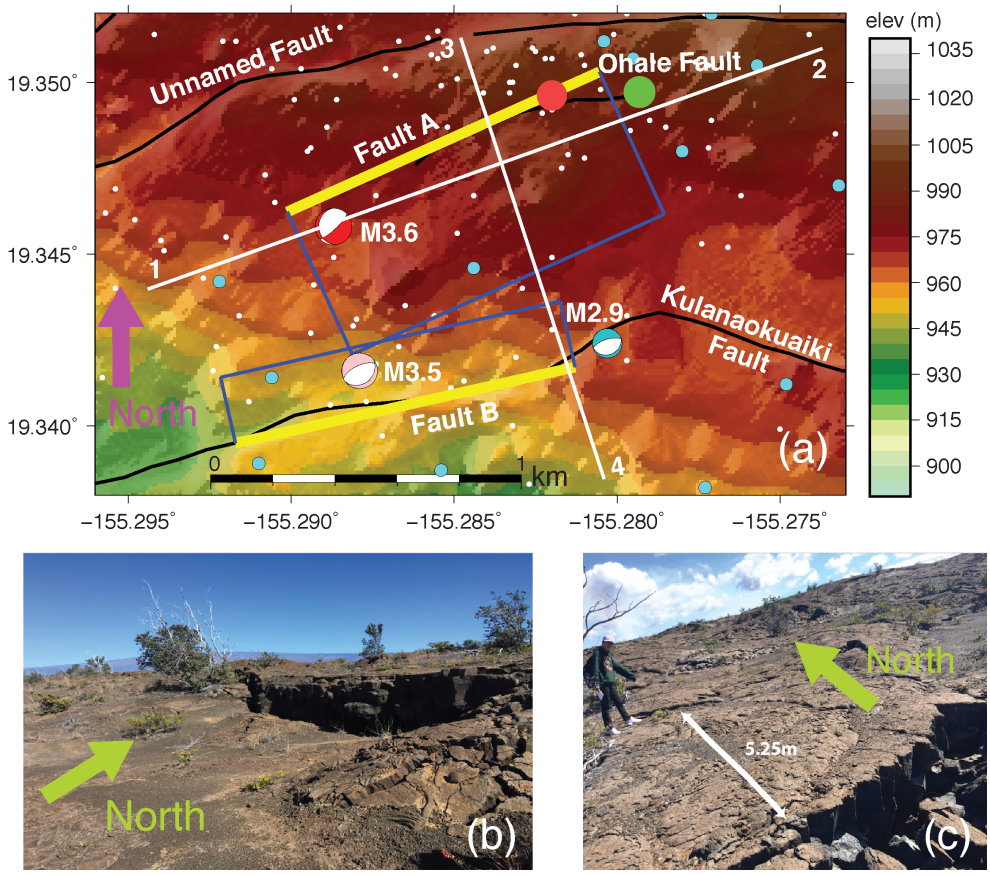

Figure 5. (a) Our two-fault model with the preferred focal solutions of the three earthquakes in the surface deformation area between the Ohale Fault and the Kulanaokuaiki Fault. Yellow solid lines are the surface projections of the upper edges of the two model dislocations, and blue lines are the other boundaries of the faults projected to the surface. White straight lines are the profiles for the cross-sections in Figure 6. The green and red circles denote the area locations in (b) and (c). (b) The major gaping fissure in the easternmost part of the Ohale Fault. The scarp facing direction is south. (c) The distance between the end of one fissure and the start of another fissure.

5 Discussion

In the following sections, we investigate and discuss possible relationships among the seismic, geodetic, and slow slip events in 2012, if there are any.

5.1 Geodetic Sources

The geodetic modeling shows that the surface deformation can be explained by slip along two faults. The first one is a 62° south-southeast dipping fault (Fault A), whose surface projection matches with the observed cracks and the south-southeast-facing scarps in the Ohale Fault area. The second one is a 77° north-northwest-dipping fault (Fault B), consistent with the north-northwest-facing scarps in the Kulanaokuaiki Fault area. We assume Fault A represents the major scarp of the Ohale Fault, and Fault B is one segment of the Kulanaokuaiki Fault. Fault A and Fault B contact each other slightly at sea level and form the boundaries of a graben.

The width of Fault B is not well constrained. We selected 1 km as our optimal estimate because a typical shallow graben model is most plausible in all the geodetic models with the same minimum RMS of the displacement residuals. There are several published estimates of the depth (relative to the ground surface) of the Koa‘e fault system. Koyanagi et al. (1972) and Duffield (1975) suggested that the fault zone might penetrate to the approximate depth of the ocean floor (~10 km). Duffield (1975) applied the “graben rule” by Hansen (1965) to calculate a depth of 667 m based on the assumption that the entire fault zone was one complex graben. Parfitt and Peacock (2001) suggested that the Koa’e fault system probably extended to a depth range from 4 km to 9 km. The graben structure with Faults A and B as two borders matches both the surface deformation and the geological observations.

5.2 Seismic Sources

The sequence of the three earthquakes (M3.5, M2.9, and M3.6) on June 5, 2012, occurred at 1.8-2.1 km depths below the ground surface as revealed by precise earthquake relocations. In Figure 6, we show these three earthquakes and the seismic velocity structure by Lin et al., (2014) along profiles 1-2 and 3-4 in Figure 5(a). The three events occurred in a zone with low Vp and

low Vp/Vs ratio (1.6 to 1.64) compared with the surrounding areas (Figure 6). These velocity properties could be explained by the presence of volatiles (Lin et al., 2014), which could increase pore pressure and reduce effective stress, thus facilitating the reactivation of pre-existing faults.

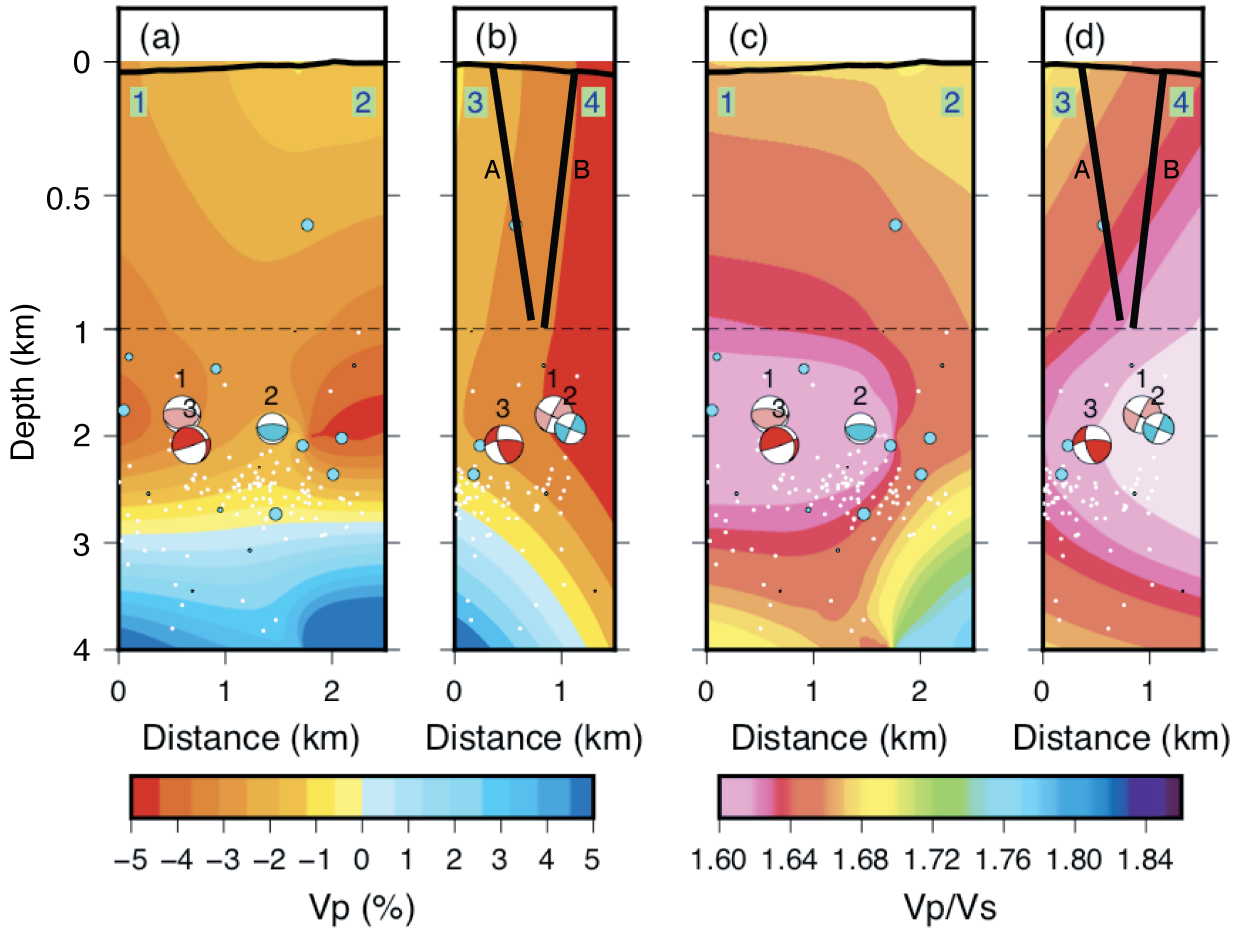

Figure 6. (a) and (b) are the Vp perturbations relative to the average value of each layer in the 3-D velocity model by Lin et al. (2014) along profiles 1-2 and 3-4 in Figure 5a. (c) and (d) are the Vp/Vs ratio model by Lin et al. (2014) along the same profiles. White dots are the background seismicity from 1992 to 2009. Cyan circles are the seismic events with 3-D relocation from 2009 to 2014. The size of each circle is proportional to the event magnitude. Two black lines indicate the fault geometry in the two-fault model from the Geodmod. The beach balls show the preferred focal solutions for the 2012 earthquake sequence (pink, blue and red beach ball for the M3.5, M2.9, and M3.6 events, respectively). Dashed horizontal lines illustrate the average sea level.

The connections between the seismic sequence and the geodetic model can be complicated due to the discrepancies between earthquake depths and modeled fault widths. The

depth of the seismic sequence is about 1 km deeper than the lower edges of the modeled elastic dislocations (Faults A and B in the two-fault model), a separation that exceeds any likely errors in our earthquake locations or geodetic modeling. The first two earthquakes share some common characteristics, including similar focal solutions and epicentral locations close to the Kulanaokuaiki Fault, implying that they might have shared the same failure source. The preferred focal solutions and the inter-event epicentral direction suggest a north-northwest-dipping source fault subparallel to Fault B. The differences in strike and dip angles between the earthquake- and deformation-based solutions are within 5° (Tables 1 and 2). If its width extended deeper along the dip direction, as suggested by previous investigations, Fault B, a fault segment or the ruptured part of the Kulanaokuaiki Fault, might be associated with the first two earthquakes.

Although the epicenter of the M3.6 earthquake is closer to Fault A, the resolved strikes from the focal solution and geodetic modeling are 30° different (Tables 1 and 2), in addition to the depth discrepancy. Therefore, we infer that this event might have occurred on another fault between the Ohale Fault and the Kulanaokuaiki Fault, instead of Fault A, which is the major scarp of the Ohale Fault.

5.3 Coulomb Stress Changes

In this section, we further examine any possible associations between the seismic and the geodetic events by evaluating the Coulomb stress changes. Because of the close time of the slow slip event on May 28, 2012, we include it in our investigation as well. If we assume the effects of pore fluids are incorporated in the normal stress change, the change in Coulomb stress $\Delta \boldsymbol{\sigma_f}$ is given by $\Delta \boldsymbol{\sigma_f} = \Delta \boldsymbol{\tau} - \boldsymbol{\mu}'(\Delta \boldsymbol{\sigma})$, where $\Delta \boldsymbol{\tau}$ is the change in shear stress along the fault of interest and $\Delta \boldsymbol{\sigma}$ is the change in normal stress along this fault, $\boldsymbol{\mu}'$ is the effective friction

coefficient (King and Stein, 1994). A positive stress change will encourage the failure of faults. We used the model of Montgomery-Brown et al. (2015) for the slow slip event (Figure 7) and calculated the changes in Coulomb failure stress using the Coulomb 3.3 software (Lin and Stein, 2004; Toda et al., 2005). High coefficients of friction (~0.8) are assumed for continental thrust faults, and very low coefficients of friction (>0.2) are considered for major transforms (Toda et al., 2011). Here we used a moderate effective friction coefficient of 0.4 for fault slips (Toda et al., 2011).

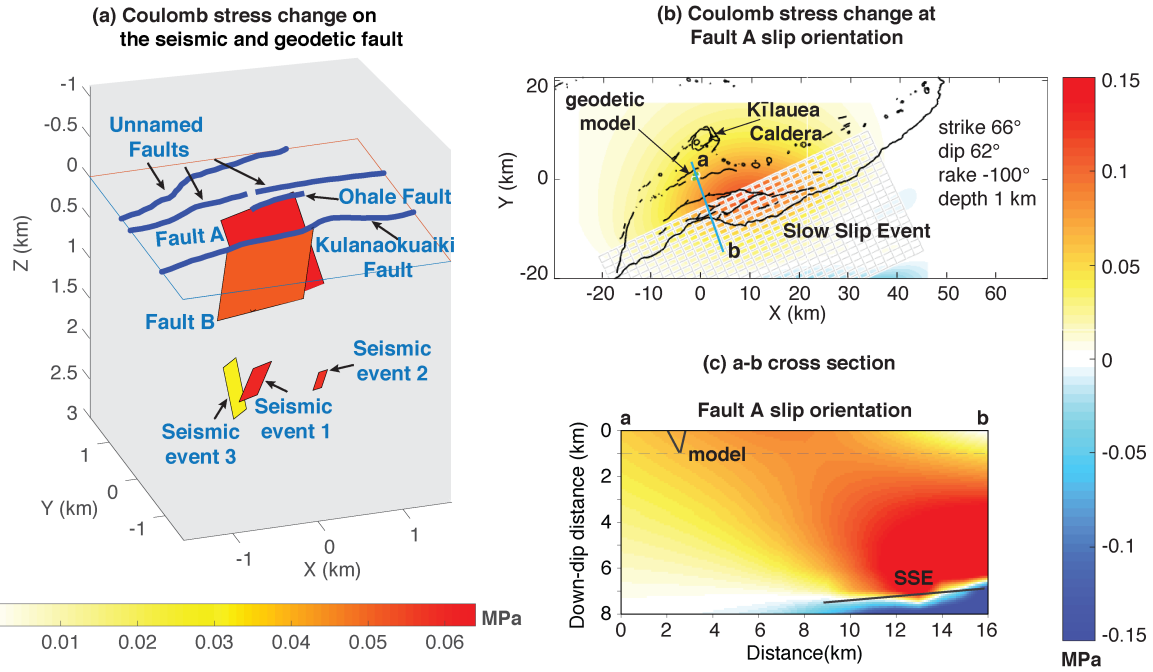

Figure 7. (a) Coulomb stress changes on both the seismic and geodetic models due to the slow slip event source. (b) Coulomb stress change on Fault A [Strike 66°, Dip 62°, Rake -100°] in its slip orientation due to the slow slip event. (c) Coulomb stress change along profile a-b due to the slow slip event on Fault A slip orientation. The positive sign of the stress change means stress increase and would encourage the failure of faults.

We calculated the fault plane parameters based on the focal solution data and empirical magnitude-area relations (Wells and Coppersmith, 1994) for the seismic events. The majority of the Coulomb stress changes due to the slow slip event were positive on both the geodetic faults (Fault A and Fault B, Figure 7) and the 18 possible fault plane solutions (see Table S1 in the supplementary material). The magnitude of the Coulomb failure stress changes (up to 0.06 MPa) is of the same order as the one that opened the East Rift Zone by the slow slip event

411 (Montgomery-Brown et al., 2015). These results suggest that the slow slip event might have
412 triggered both the geodetic and the seismic events.

413 In order to investigate whether the seismic events may have triggered the geodetic events
414 or vice-versa, we calculated the respective stress changes using the seismic faults as source faults
415 and the geodetic faults as receiver faults, and vice versa. We found that for all the source-
416 receiver configurations, the majority of the Coulomb stress changes were negative or close to
417 zero in our preferred seismic focal planes (see supplementary text S2, S5, and tables S2-S5). The
418 absence of any configuration with positive stress changes argues against the triggering
419 mechanism between these two types of events.

420 For the two geodetic events, the stress changes from the slip of Fault A on Fault B and
421 vice versa were both positive. Although this suggests that slips on both geodetic faults might
422 have influenced each other, unfortunately, our data are unable to constrain their time
423 relationship.

424

425 **5.4 Hypothesis**

426 The relationship between the fault slip in the two-fault model and the sequence of seismic
427 events is ambiguous. The stress changes do not support a direct influence between them
428 (supplementary text S5). Furthermore, the unclear time relation of these events makes it difficult
429 to discern any interaction. The earthquakes occurred on June 5, 2012. The surface deformation
430 was observed between June 2 and June 8 2012. It is possible for the seismic sequence to occur
431 before, during, or after the surface deformation. We also cannot imply the time relation of the
432 two geodetic slips based on the seismic sequence because we do not interpret the M3.6

earthquake to have occurred on either Fault A or B. However, it seems clear that the influence between them was much less than that exerted by the 2012 slow slip event from the perspective of the stress change.

We hypothesize that all the investigated events started with the slow slip event in late May 2012 (Figure 8a). The initial stress state under the Koa‘e fault system is generally tensile. We assume the stress state is expressed as numerous cracks underground (Figure 8b) based on the observed cracks at the surface in the Ohale Fault area and the scaled physical models of the normal fault system in basalt (Holland et al., 2006). The slow slip event triggered the fault slip by increasing the Coulomb stress in the normal or nearly normal rake direction of the fault planes in the two-fault model (Figure 8c). It also increased the stress in the area of the three seismic events beneath the Ohale and the Kulanaokuaiki Faults. With the presence of the long-term tensile stress and the positive Coulomb stress change due to the slow slip event, the first two seismic events could result from the reactivation of the pre-existing faults, which could be the sub-faults of the Kulanaokuaiki Fault (Figure 8c). Both the seismic events and the slips on the surface faults are expressions of the evolution of the Koa‘e fault system.

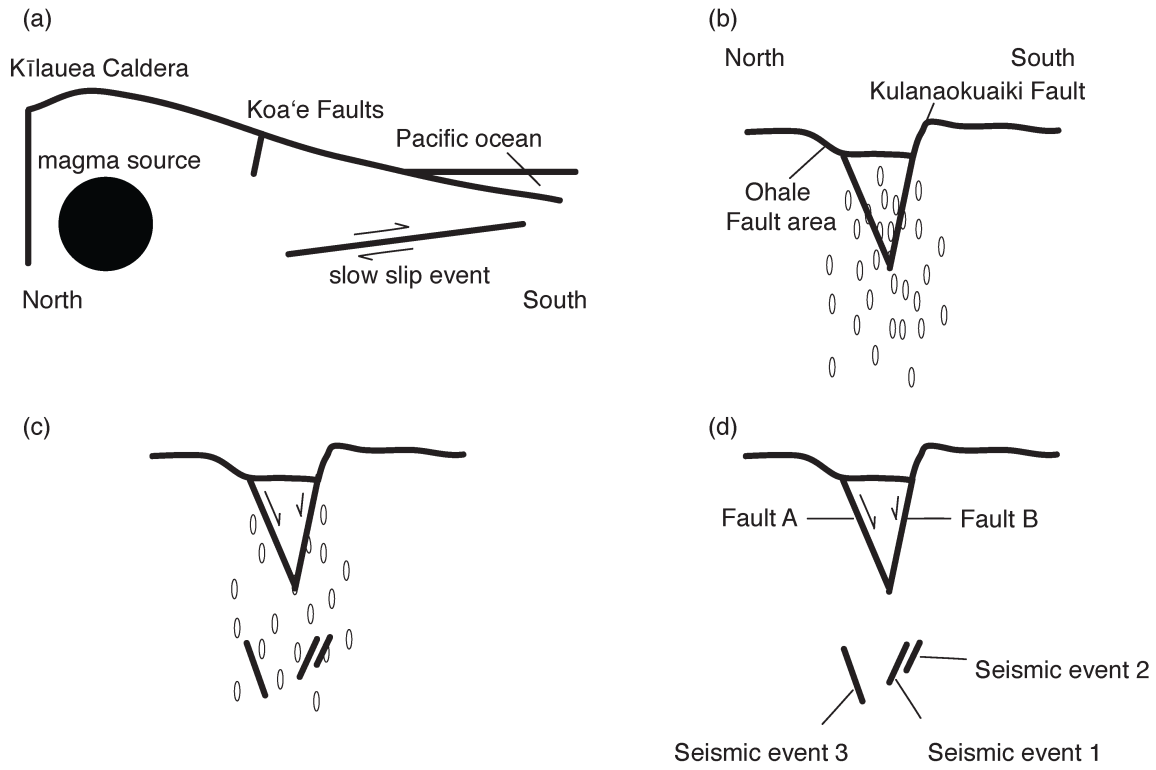

Figure 8. (a) A cartoon illustrating the depth profile of the 2012 slow slip event and the Koa'e fault system. (b) The conceptual state beneath the Ohale Fault area and the Kulanaokuaiki Fault before the 2012 slow slip event. Numerous cracks exist due to the extensional environmental stress state. (c) The conceptual state beneath the Ohale Fault area and the Kulanaokuaiki Fault during and after the 2012 slow slip event. Two major faults, forming the graben structure, slipped in the normal rake. Meanwhile, pre-existing faults (e.g., the sub-faults of the Kulanaokuaiki Fault) slipped at ~2 km below the ground surface, expressed as the seismic sequence. (d) Our two-fault geodetic model and the preferred focal planes of the three seismic events. Note that the scales in this figure are only for illustration and are not proportional to real structures.

Here we consider the southward moving part of Kīlauea volcano from the surface of the south flank to the décollement fault at the base of the volcano edifice as one whole geological structure to assist our investigation on the multiple events of 2012: (1) the slow slip event, (2) the surface deformation, and (3) the shallow seismic sequence. This structure contains the area where all the above events and the associated stress fields occur. If we only consider these three types of events within this structure, the slow slip event is the direct cause of the following seismic sequence and geodetic observations. However, we need to take the influence of other

events (e.g., magma movement or gravitational spreading) within the evolving Kīlauea volcano into consideration. Magma intrusions and rift openings can encourage the décollement fault toward failure and trigger slow slip events (Montgomery-Brown et al., 2015). One recent example is the slow slip event in June 2007 triggered by an East Rift Zone intrusion and followed by rift opening (Montgomery-Brown et al., 2015). Moreover, slow slip events can be caused by the gravitational sliding on the décollement fault (Delaney et al., 1998; Montgomery-Brown, et al., 2009). Thus we can attribute the cause of both the seismic sequence and the surface deformation to the overall magmatic system, in which the Koa‘e fault system evolves, accommodating the south flank motion continuously. The large-scale events (e.g., slow slip events) play a role in accelerating this evolution.

The cumulative annual secular motion of the south flank is up to ~8 cm/yr (Owen et al., 2000; Miklius et al., 2005). Both seismic (i.e., earthquakes) and aseismic (e.g., magmatic intrusions and slow slip) events contribute to the cumulative annual motion. In this paper, we mainly discuss the relationships among the events in a relatively short period from May to June 2012, excluding the secular motion. In the long-term evolution of the Koa‘e fault system, the secular motion exerts similar stress accumulation and release on the Koa‘e due to the same moving direction and the similar mass of motion compared with the slow slip events. It is essential for the evolution of the Koa‘e fault system. However, the influence from the secular motion is long-term, small scale in the short time interval (several days) and difficult to identify and explore.

5.5 Complications and Solutions

Our geodetic model represents the latest InSAR analysis for the Koa‘e. However, it is worth pointing out two complications. The first one is the inconsistency of the dip angles

between the geodetic modeled faults (62-77°) and the observed faults in the walls of pit craters (80-90°). The field observations demonstrate the dip angles of the faults at the surface, but our model simulates the dip angles at depth, which might be different from the surface extension. Scaled model experiments (Holland et al., 2006) will be helpful to examine and validate our two-fault model in the future. Another complication is the poorly constrained width of Fault B. The cause could be the small deformation signal in both near-field and far-field areas at the phase discontinuity (Figure 2c and d) near the Kulanaokuaiki Fault. The variable width makes the relationship ambiguous between the seismic sequence and the slip of Fault B. We will continue to investigate the geodetic model in our future work when more InSAR data become available, especially on the width of Fault B or the depth of the Kulanaokuaiki Fault.

6 Conclusions

In this paper, we combine geophysical analyses from seismic, InSAR, GPS data, and field observations to interpret a sequence of geophysical phenomena, including the 2012 slow slip event, the June 2012 earthquake sequence, and the surface deformation. We provide an explicit subsurface geometric structure of the two-fault model in the area of the Ohale and the Kulanaokuaiki Faults and estimate the depth (~1 km) of the Ohale Fault. In our model, the Ohale Fault and one segment of the Kulanaokuaiki Fault come in contact at sea level and form the borders of a graben between them. Our results suggest that the slow slip event might have served as a triggering event for the shallow sequence of earthquakes ~2 km deep below the ground surface and the slips on the two faults. This interference implies that in the complex and evolving Koa‘e system, different types of geophysical events could influence each other. At Kīlauea, although the stress influence from the base of the volcano edifice to the surface of the south flank, including magma intrusion and gravitational spreading, dominates the evolution of the

Koa‘e fault system, slow slip events may play a triggering role in accelerating it. As part of the boundary between the moving south flank and the stable main part of the volcano edifice, the Koa‘e fault system and the East Rift Zone are the most active parts in the entire evolution of Kīlauea. In May 2018, the European Space Agency’s Sentinel-1 showed another fringe pattern in the Koa‘e fault system, which will help explore the features of Koa‘e subsurface structures in our future work.

Acknowledgments

Seismic data used in this study were obtained and originated from the USGS HVO (https://volcanoes.usgs.gov/observatories/hvo/). Previous velocity models, location catalogs, and computational software were collected from published studies listed in the references. InSAR data for this study were accessed through the Hawaiian Volcano Supersite (https://geo-gsnl.org/) and the Italian Space Agency. GPS data were downloaded from the Nevada Geodetic Laboratory (http://geodesy.unr.edu/magnet.php). We thank Emily Montgomery-Brown for making the 2012 slow slip event digital model available and Stephen Martel for sharing the detailed geological map of the Koa‘e fault system. We also thank Anieri Morales Rivera and Sara Mirzaee for their discussions in the InSAR data process. We are grateful to Michael Poland, Emily Montgomery-Brown, Ingrid Johanson, the Associate Editor, and an anonymous reviewer for their detailed and constructive comments. All the Coulomb stress calculations were made in Coulomb 3.3 deformation and stress-change software. This research work was supported by the National Science Foundation grants EAR-1246935 and EAR-1928158. Shuangyu Ge’s fieldwork was

partially supported by the Kleinman Grant for Volcano Research. Figures were made using GMT (http://gmt.soest.hawaii.edu/) and Matlab (https://www.mathworks.com/).

References

Árnadóttir, T., P. Segall, and P. Delaney (1991), A fault model for the 1989 Kīlauea south flank earthquake from leveling and seismic data, *Geophysical Research Letters*, *18*(12), 2217–2220.

Avery, V.F., R.S. Fiske, and D.A. Swanson (2002), Leveling, EDM, and crack-monitoring networks in the Koa‘e fault system, Kīlauea Volcano, Hawai‘i, *U.S. Geological Survey Open-File Report,* 02-129.

Baker, S., and F. Amelung (2012), Top-down inflation and deflation at the summit of Kīlauea Volcano, Hawai‘i observed with InSAR, *Journal of Geophysical Research: Solid Earth*, *117*(B12).

Battaglia, J., J.-L. Got, and P. Okubo (2003), Location of long-period events below Kīlauea Volcano using seismic amplitudes and accurate relative relocation, *Journal of Geophysical Research, 108*(B12), 2553.

Borgia, A., P. T. Delaney, and R. P. Denlinger (2000), Spreading volcanoes, *Annual Review of Earth and Planetary Sciences*, *28*(1), 539–570.

Boxenbaum, H. G., S. Riegelman, and R. M. Elashoff (1974), Statistical estimations in pharmacokinetics, *Journal of Pharmacokinetics and Biopharmaceutics, 2*(2), 123–148

Brooks, B. A., and L. Neil Frazer (2005), Importance reweighting reduces dependence on temperature in Gibbs samplers: An application to the coseismic geodetic inverse problem, *Geophysical Journal International*, *161*(1), 12–20.

Bubeck, A., R. Walker, C. MacLeod, and J. Imber (2014), Rift fault geometry and distribution in layered basaltic rocks: A comparison between the Koa‘e (Hawai‘i) and Krafla (Iceland) fault systems, in *AGU Fall Meeting Abstracts*.

Cannon, E. C., R. Burgmann, and S. E. Owen (2001), Shallow normal faulting and block rotation associated with the 1975 Kalapana earthquake, Kīlauea Volcano, Hawai‘i, *Bulletin of the Seismological Society of America, 91*(6), 1553–1562.

Cayol, V., J. H. Dieterich, A. T. Okamura, and A. Miklius (2000), High magma storage rates before the 1983 eruption of Kīlauea, Hawai‘i, Science, 288(5475), 2343–2346.

565 Delaney, P., Denlinger, R., Lisowski, M., Miklius, A., Okubo, P., Okamura, A., and Sako, M.
566 (1998), Volcanic spreading at Kilauea, 1976-1996, *Journal of Geophysical Research: Solid*
567 *Earth*, 103(B8):18003–18023.

568 Denlinger, R. P., and P. Okubo (1995), Structure of the mobile south flank of Kīlauea volcano,
569 Hawai‘i, *Journal of Geophysical Research: Solid Earth*, *100*(B12), 24,499–24,507.

570 Duffield, W. A. (1975), Structure and origin of the Koa‘e fault system, Kīlauea Volcano,
571 Hawai‘i, *US Geological Survey*, *Professional Paper* 856.

572 Gillard, D., A. M. Rubin, and P. Okubo (1996), Highly concentrated seismicity caused by
573 deformation of Kīlauea’s deep magma system, *Nature, 384*(6607), 343.

574 Got, J.-L., and P. Okubo (2003), New insights into Kīlauea’s volcano dynamics brought by
575 large-scale relative relocation of microearthquakes, *Journal of Geophysical Research: Solid*
576 *Earth, 108*(B7).

577 Got, J.-L., J. Fréchet, and F. W. Klein (1994), Deep fault plane geometry inferred from multiplet
578 relative relocation beneath the south flank of Kīlauea, *Journal of Geophysical Research: Solid*
579 *Earth, 99*(B8), 15,375–15,386.

580 Hansen, W. R. (1965), Effects of the earthquake of March 27, 1964, at Anchorage, Alaska, US
581 *Geological Survey*, *Professional Paper* 542-A, p.A1-A68.

582 Hardebeck, J. L., and P. M. Shearer (2002), A new method for determining first-motion focal
583 mechanisms, *Bulletin of the Seismological Society of America*, *92*(6), 2264–2276.

584 Holland, M., J. L. Urai, and S. Martel (2006), The internal structure of fault zones in basaltic
585 sequences, *Earth and Planetary Science Letters*, *248*(1-2), 301–315.

586 King, G. C., R. S. Stein, and J. Lin (1994), Static stress changes and the triggering of
587 earthquakes, *Bulletin of the Seismological Society of America*, *84*(3), 935–953.

588 Klein, F. W., R. Y. Koyanagi, J. S. Nakata, and W. R. Tanigawa (1987), The seismicity of
589 Kīlauea’s magma system, *US Geological Survey*, *Professional Paper*, *1350*(2), 1019–1185.

590 Koyanagi, R., D. Swanson, and E. Endo (1972), Distribution of earthquakes related to mobility
591 of the south flank of Kīlauea volcano, Hawai‘i. *Geological Survey Research 1972, US*
592 *Geological. Survey. Professional. Paper.*

593 Lin, G. (2018), The source-specific station term and waveform cross-correlation earthquake
594 location package and its applications to California and New Zealand, *Seismological Research*
595 *Letters*, *89*(5), 1877–1885.

596 Lin, G., and P. G. Okubo (2016), A large refined catalog of earthquake relocations and focal
597 mechanisms for the Island of Hawai‘i and its seismotectonic implications, *Journal of*
598 *Geophysical Research: Solid Earth*, *121*(7), 5031–5048.

599 Lin, G., P. M. Shearer, and E. Hauksson (2007), Applying a three-dimensional velocity model,
600 waveform cross-correlation, and cluster analysis to locate southern California seismicity from
601 1981 to 2005, *Journal of Geophysical Research: Solid Earth*, *112*(B12), 2156-2202.

602 Lin, G., P. M. Shearer, R. S. Matoza, P. G. Okubo, and F. Amelung (2014), Three-dimensional
603 seismic velocity structure of Mauna Loa and Kīlauea Volcanoes in Hawai‘i from local seismic
604 tomography, *Journal of Geophysical Research: Solid Earth*, *119*(5), 4377–4392.

605 Lin, J., and R. S. Stein (2004), Stress triggering in thrust and subduction earthquakes and stress
606 interaction between the southern San Andreas and nearby thrust and strike-slip faults, *Journal of*
607 *Geophysical Research: Solid Earth*, *109*(B2).

608 Lipman, P. W., J. P. Lockwood, R. T. Okamura, D. A. Swanson, and K. M. Yamashita (1985),
609 Ground deformation associated with the 1975 magnitude-7.2 earthquake and resulting changes in
610 activity of Kīlauea Volcano, Hawai‘i. *US Geological Survey, Professional Paper,* 1276, (45 pp).

611 Ludden, T. M., S. L. Beal, and L. B. Sheiner (1994), Comparison of the Akaike Information
612 Criterion, the Schwarz Criterion and the F test as guides to model selection, *Journal of*
613 *Pharmacokinetics and Biopharmaceutics, 22*(5), 431–445.

614 Martel, S. J., and J. S. Langley (2006), Propagation of normal faults to the surface in basalt,
615 Koa‘e fault system, Hawai‘i, *Journal of Structural Geology*, *28*(12), 2123–2143.

616 Matoza, R. S., P. M. Shearer, G. Lin, C. J. Wolfe, and P. G. Okubo (2013), Systematic relocation
617 of seismicity on Hawai‘i island from 1992 to 2009 using waveform cross correlation and cluster
618 analysis, *Journal of Geophysical Research: Solid Earth, 118*(5), 2275–2288.

619 Menke, W. (1989), *Geophysical data analysis: Discrete inverse theory, Revised Edition*
620 (Academic Press, Inc., New York).

621 Miklius, A., P. Cervelli, M. Sako, M. Lisowski, S. Owen, P. Segal, J. Foster, K. Kamibayashi,
622 and B. Brooks (2005), Global positioning system measurements on the Island of Hawai’i: 1997
623 through 2004, U.S. Geological Survey Open-File Report, 2005-1425, 48 pp.

624 Montgomery-Brown, E. K., Segall, P., and Miklius, A. (2009), Kilauea slow slip events:
625 Identification, source inversions, and relation to seismicity, Journal of Geophysical Research:
626 Solid Earth, 114:B00A03, doi:10.1029/2008JB006074.

627 Montgomery-Brown, E., C. Thurber, C. Wolfe, and P. Okubo (2013), Slow slip and tremor
628 search at Kīlauea Volcano, Hawai‘i, *Geochemistry, Geophysics, Geosystems*, *14*(2), 367–384

629 Montgomery-Brown, E. K., M. P. Poland, and A. Miklius (2015), A delicate balance of
630 magmatic-tectonic interaction at Kīlauea Volcano, Hawai‘i, revealed from slow slip events,
631 *Hawaiian Volcanoes: From Source to Surface*, pp. 269–288.

632 Okada, Y. (1992), Internal deformation due to shear and tensile faults in a half-space, *Bulletin of*
633 *the Seismological Society of America*, *82*(2), 1018–1040.

Owen,S., P. Segall, M. Lisowski, A. Miklius, R. Denlinger, J. Freymueller, T. Arnadóttir, and M. Sako, Rapid deformation of Kīlauea Volcano: Global Positioning System measurements between 1990 and 1996, *Journal of Geophysical Research, 105*, 18,983-18998, 2000.

Parfitt, E., and D. Peacock (2001), Faulting in the south flank of Kīlauea Volcano, Hawai‘i, *Journal of Volcanology and Geothermal Research, 106*(3-4), 265–284.

Park, J., J. K. Morgan, C. A. Zelt, and P. G. Okubo (2009), Volcano-tectonic implications of 3-d velocity structures derived from joint active and passive source tomography of the island of Hawai‘i, *Journal of Geophysical Research: Solid Earth, 114*(B9).

Peacock, D., and E. Parfitt (2002), Active relay ramps and normal fault propagation on Kīlauea Volcano, Hawai‘i, *Journal of Structural Geology*, *24*(4), 729–742.

Plattner, C., F. Amelung, S. Baker, R. Govers, and M. Poland (2013), The role of viscous magma mush spreading in volcanic flank motion at Kīlauea Volcano, Hawai‘i, *Journal of Geophysical Research: Solid Earth*, *118*(5), 2474–2487.

Podolsky, D. M., and G. P. Roberts (2008), Growth of the volcano-flank Koa‘e fault system, Hawai‘i, *Journal of Structural Geology*, *30*(10), 1254–1263.

Richards-Dinger, K., and P. Shearer (2000), Earthquake locations in southern California obtained using source-specific station terms, *Journal of Geophysical Research: Solid Earth*, *105*(B5), 10,939–10,960.

Rosen, P. A., E. Gurrola, G. F. Sacco, and H. Zebker (2012), The Insar scientific computing environment, in *EUSAR 2012; 9th European Conference on Synthetic Aperture Radar*, pp. 730–733, VDE.

Rubin, A. M., D. Gillard, and J.-L. Got (1998), A reinterpretation of seismicity associated with the January 1983 dike intrusion at Kīlauea volcano, Hawai‘i, *Journal of Geophysical Research: Solid Earth, 103*(B5), 10,003–10,015.

Shearer, P., E. Hauksson, and G. Lin (2005), Southern California hypocenter relocation with waveform cross-correlation, Part 2: Results using source-specific station terms and cluster analysis, *Bulletin of the Seismological Society of America*, *95*(3), 904–915.

Swanson, D.A., Fiske, R.S., Thornber, C.R., and Poland, M.P. (2018), Dikes in the Koa‘e fault system, and the Koa‘e-East Rift Zone structural grain at Kīlauea Volcano, Hawai‘i, in Poland, M., Garcia, M., Camp, V., and Grunder, A., eds., *Field Volcanology: A Tribute to the Distinguished Society of America Special Paper 538*, p. 247-274, https://doi.org/10.1130/2018.2538(11).

Syracuse, E. M., C. H. Thurber, C. J. Wolfe, P. G. Okubo, J. H. Foster, and B. A. Brooks (2010), High-resolution locations of triggered earthquakes and tomographic imaging of Kīlauea volcano’s south flank, *Journal of Geophysical Research: Solid Earth*, *115*(B10).

Tilling, R. I., and J. J. Dvorak (1993), Anatomy of a basaltic volcano, *Nature, 363*(6425), 125.

Toda, S., R. S. Stein, K. Richards-Dinger, and S. B. Bozkurt (2005), Forecasting the evolution of seismicity in southern California: Animations built on earthquake stress transfer, *Journal of Geophysical Research: Solid Earth*, *110*(B5).

Toda, S., R. S. Stein, V. Sevilgen, and J. Lin (2011), Coulomb 3.3 graphic-rich deformation and stress-change software for earthquake, tectonic, and volcano research and teaching-user guide, *US Geological Survey Open-File Report,* 2011-1060, 63 pp.

Wells, D., and K. Coppersmith (1994), New empirical relationships among magnitude, rupture length, rupture width, rupture area and surface displacement, *Bulletin of the Seismological Society of America, 84*(4), 974–1002.

Wolfe, E. W., and J. Morris (1996), *Geological map of the Island of Hawai'i,* 2524-A.

Wolfe, C. J., P. G. Okubo, and P. M. Shearer (2003), Mantle fault zone beneath Kīlauea volcano, Hawai'i, *Science, 300*(5618), 478–480.

Wolfe, C. J., P. G. Okubo, G. Ekström, M. Nettles, and P. M. Shearer (2004), Characteristics of deep (≥ 13 km) Hawaiian earthquakes and Hawaiian earthquakes west of 155.55° W, *Geochemistry, Geophysics, Geosystems, 5*(4).

Wolfe, C. J., B. A. Brooks, J. H. Foster, and P. G. Okubo (2007), Microearthquake streaks and seismicity triggered by slow earthquakes on the mobile south flank of Kīlauea volcano, Hawai'i, *Geophysical Research Letters, 34*(23).

Wright, T. L., and F. W. Klein (2006), Deep magma transport at Kīlauea volcano, Hawai'i, *Lithos*, *87*(1-2), 50–79.